THE JOURNAL OF PHYSICAL CHEMISTRY B

Article

pubs.acs.org/JPCB

Quantitative Determination of Lateral Concentration and Depth Profile of Histidine-Tagged Recombinant Proteins Probed by Grazing Incidence X-ray Fluorescence

Alexander Körner,[†] Wasim Abuillan,[†] Christina Deichmann,[‡] Fernanda F. Rossetti,[†,⊥] Almut Köhler,[‡] Oleg V. Konovalov,[§] Doris Wedlich,[‡] and Motomu Tanaka*[,†,∥,⊥]

[†]Physical Chemistry of Biosystems, Physical Chemistry Institute, University of Heidelberg, 69120 Heidelberg, Germany

[‡]Cell and Developmental Biology, Zoological Institute, Karlsruhe Institute of Technology (KIT), 76131 Karlsruhe, Germany

[§]European Synchrotron Radiation Facility (ESRF), Grenoble Cedex 9 38053, France

[∥]Cell Biophysics Laboratory, Institute of Toxicology and Genetics, Karlsruhe Institute of Technology (KIT), 76021 Karlsruhe, Germany

[⊥]Institute for Integrated Cell-Material Sciences (WPI iCeMS), Kyoto University, 606-8501 Kyoto, Japan

Supporting Information

ABSTRACT: We have demonstrated that the complementary combination of grazing incidence X-ray fluorescence (GIXF) with specular X-ray reflectivity (XRR) can be used to quantitatively determine the density profiles of Ni^{2+} ions complexed with chelator headgroups as well as S atoms in recombinant proteins anchored to lipid monolayers at the air/water interface. First, we prepared phospholipid monolayers incorporating chelator lipid anchors at different molar fractions at the air/water interface. The fine-structures perpendicular to the global plane of monolayers were characterized by XRR in the presence of Ni^{2+} ions, yielding the thickness, roughness, and electron density of the stratified lipid monolayers. X-ray fluorescence intensities from Ni Kα core levels recorded at the incidence angles below and above the critical angle of total reflection allow for the determination of the position and lateral density of Ni^{2+} ions associated with chelator headgroups with a high spatial accuracy (±5 Å). The coupling of histidine-tagged *Xenopus* cadherin 11 (Xcad-11) can also be identified by changes in the fines-structures using XRR. Although fluorescence intensities from S Kα level were much weaker than Ni Kα signals, we could detect the location of S atoms in recombinant Xcad-11 proteins.

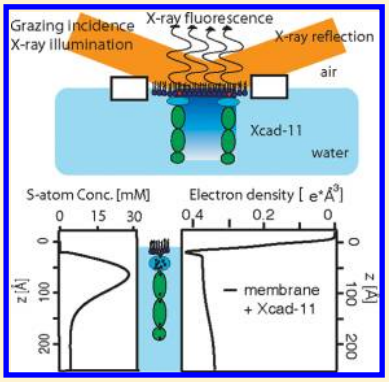

INTRODUCTION

Bilayer lipid membranes are vital components of biological membranes, defining the outer boundary of living cells or of internal cell compartments. They do not only act as smart filters to selectively import/export materials but also play major roles in many key biochemical reactions such as signal transduction processes and cell−cell interactions.

To date, lipid monolayers deposited at the air/water interface have intensively been used as a defined model system suited to study the phase transition and lateral phase separation.[1−3] Moreover, changes in the fine-structures perpendicular to the membrane plane caused by the coupling of membrane-interacting molecules can sensitively be detected by reflectivity-based techniques, such as ellipsometry and Brewster angle microscopy.[4−6] Specular X-ray reflectivity (XRR) and neutron reflectivity (NR) offer a unique advantage that they can provide with not only thickness and refractive index (i.e., scattering length density) but also the Gaussian roughness of stratified layers with sub-Å accuracy.

Modern protein biochemistry enables one to engineer various recombinant proteins with different "tags" (e.g., histidine, biotin, and snap tags), which can readily be purified by affinity chromatography.[7−10] In the case of histidine-tagged proteins, chelator complexes of nitrilotriacetic acid (NTA) groups and divalent metal ion, for example, Ni^{2+}, Zn^{2+}, and Cu^{2+}, that are covalently linked to solid matrices[11] or lipid head groups[12] have widely been used as high affinity anchors for recombinant proteins tagged with histidines.

The coupling of recombinant proteins with his-tags to monolayer surfaces incorporating NTA-functionalized lipids can be detected by ellipsometry or XRR/NR at the air/water interface. However, the analysis of experimental results with slab models often creates artifacts, when (i) the lateral protein densities are low and (ii) the orientation of proteins are not fully known.

In this study, we propose that the combination of XRR and GIXF allows for the quantitative determination of (A) the yield of chelator complex formation in monolayers containing NTA

Received: February 22, 2013
Revised: April 4, 2013
Published: April 15, 2013

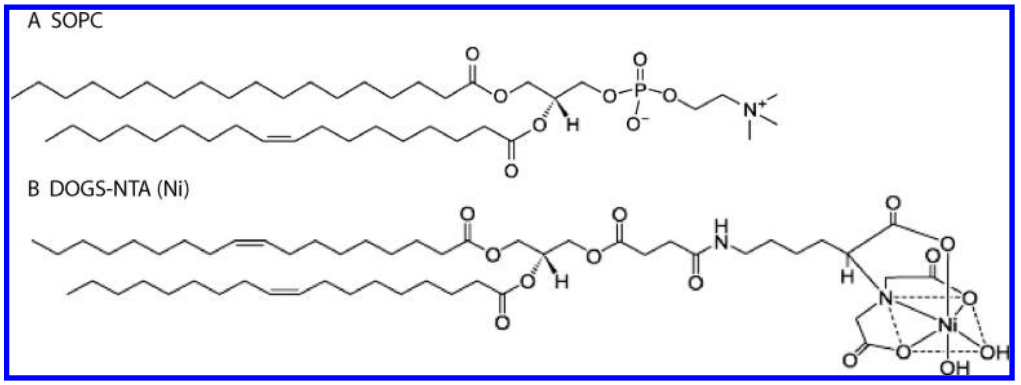

Figure 1. Structure of SOPC (A) and DOGS-NTA (Ni) (B).

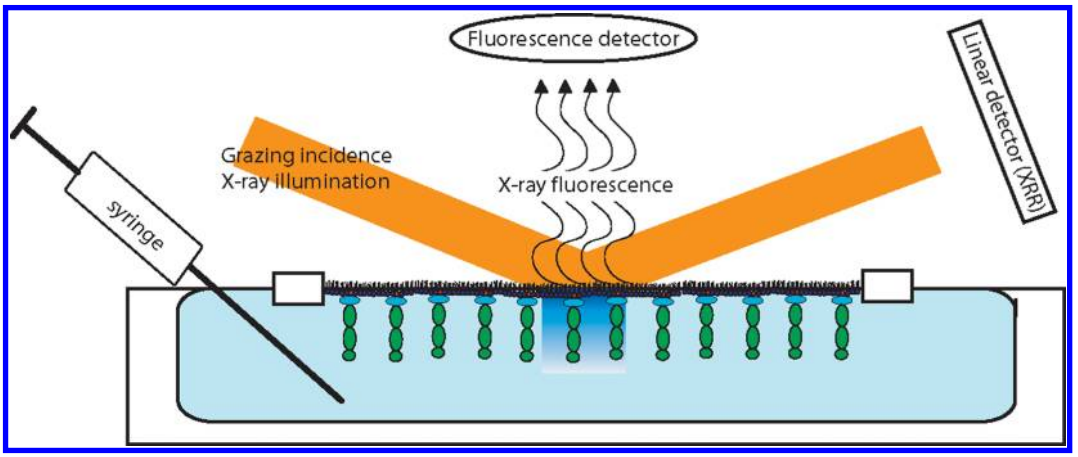

Figure 2. The experimental setup and the scattering geometry used for XRR and GIXF.

lipids in the presence of Ni ions, and (B) the conformation and lateral density of histidine-tagged proteins. We deposited monolayers of stearoyl-oleoyl-phosphatidylcholine (SOPC) incorporating NTA lipids at different molar fractions at the air/water interface, and measured XRR and GIXF simultaneously. The analysis of XRR yields the thickness, electron density, and roughness of hydrocarbon chains and head groups, and the electronic structures of monolayers obtained from XRR are essential for the calculation of illumination profiles of electromagnetic waves in thin, stratified systems. This enabled one to quantitatively calculate the intensity of reflected and refracted beams and thus the concentration profile of Ni^{2+} ions perpendicular to the membrane plane.

In the second part, the monolayer systems were characterized after the coupling of recombinant proteins with histidine tags. Here, monolayers were functionalized with histidine-tagged, extracellular domains (EC1-3) of *Xenopus* cadherin 11 (Xcad-11), which plays key roles in cell adhesion and migration of Neural crest cells (NCC).[13] The fine structure of the monolayer displaying Xcad-11 was measured by XRR and the successful coupling to the Ni-NTA complex was confirmed by the localization of the protein's sulfur atoms using GIXF.

MATERIALS AND METHODS

Materials and Sample Preparation. KCl, EDTA, and $CHCl_3$ were purchased from Sigma-Aldrich (Germany) and Hepes, $NiCl_2$, and $CaCl_2$ from Carl Roth GmbH (Germany). Double deionized water (Milli-Q, Molsheim) with a specific resistance of $\rho > 18$ MΩcm was used to prepare "Ni^{2+}-free buffer" (Hepes-buffered saline (HBS) containing 100 mM KCl, 5 mM Hepes, pH 7.4) and "Ni^{2+}-loaded buffer" that contains 5 mM $NiCl_2$ in addition (pH 7.4). The 1-stearoyl-2-oleoyl-sn-glycero-3-phosphocholine (SOPC, Figure 1A), 1,2-dioleoyl-sn-glycero-3-[(N-(5-amino-1-carboxypentyl)-iminodiacetic acid)-succinyl] (nickel salt) (DOGS-NTA (Ni^{2+}), Figure 1B), obtained from Avanti Polar Lipids (Alabaster, AL), were dissolved in $CHCl_3$ at a concentration of 1 mg/mL. SOPC solutions containing different molar fractions of DOGS-NTA (5, 25, and 50 mol %) were prepared for the following experiments.

Lipid monolayers were prepared by the deposition of lipid solutions onto Ni^{2+}-free or Ni^{2+}-loaded buffer. After 20 min of solvent evaporation, the film was compressed to a surface pressure of $\pi = 20$ mN/m. *Xenopus* cadherin 11 EC 1-3 Snap His12 (Xcad-11)[13,14] was synthesized by fusing the extracellular domain 1−3 (EC1-3) of Xcad-11 (subcloned in pSEMS1-26m (Covalys, Germany)) to a mutated hAGT protein[15] and 12 histidins, and was dissolved in Ni^{2+}-free buffer at a concentration of 40 μg/mL. The coupling of Xcad-11 to lipid monolayers was achieved by the injection of Xcad-11 under the monolayer.

XRR and GIXF experiments. XRR and GIXF experiments were carried out at the beamline ID10B of the European Synchrotron Radiation Facility (ESRF, Grenoble). The samples were irradiated with a monochromatic synchrotron beam with an energy of 9 keV ($\lambda = 1.38$ Å). The film balance was kept in He atmosphere to reduce the scattering of fluorescence emission from air. Figure 2 represents a schematic drawing of the experimental setup used for the simultaneous XRR and GIXF experiments.

dx.doi.org/10.1021/jp401869t | J. Phys. Chem. B 2013, 117, 5002−5008

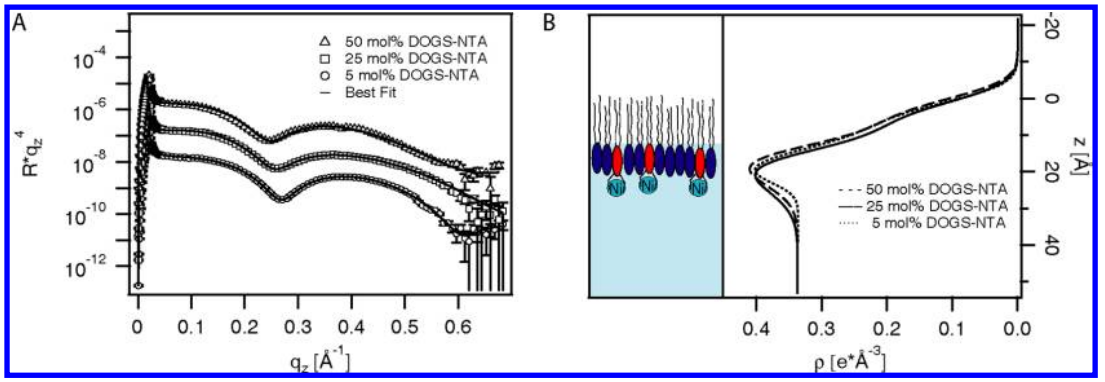

Figure 3. (A) XRR results of SOPC monolayers incorporating 5 mol % (open circles), 25 mol % (open squares), and 50 mol % (open triangles) DOGS-NTA on Ni^{2+}-loaded buffer. The best fits corresponding to the experimental results are presented as solid lines. (B) The reconstructed electron density profiles in the direction perpendicular to the air/water interface.

XRR was measured with a linear detector (Vantec-1, Bruker AXS, U.S.A.) by integrating the pixels near the specular plane, and the background was subtracted by integrating the intensity out of the specular plane (see Supporting Information). The reflectivity was normalized to the incident beam and analyzed using the Parratt formalism[16] with a genetic minimization algorithm implemented in the MOTOFIT software package.[17] The incident angle α_i was transformed into the scattering vector component normal to the interface, $q_z = [(4\pi)/\lambda]\sin\alpha_i$.

GIXF measurements were carried out at incident angles α_i below and above the critical angle of total reflection, is α_c = 0.138°. Here, the penetration depth of the evanescent field depends on the angle of incidence[18]

$$\Lambda(\alpha_i) = \frac{\lambda}{\sqrt{8}\pi}[\sqrt{(\alpha_i^2 - \alpha_c^2)^2 + 4\beta^2} - (\alpha_i^2 - \alpha_c^2)]^{-1/2} \quad (2)$$

where β is the imaginary part of the refractive index $n = 1 - \delta + i\beta$.

X-ray fluorescence signals from elements in the illuminated volume were recorded with an energy sensitive detector (Vortex, SII NanoTechnology, U.S.A.) and normalized by the detector counting efficiency. Subsequently, the intensities were normalized by the intensity of elastically scattered beam to compensate systematic differences between the experiments. In the last step, the fluorescence signals in the presence of monolayers were normalized by the signals from the blank buffer. This procedure avoids artifacts arising from the experimental geometry, such as the size of beam footprint and the fluorescence detector aperture.

Fluorescence Intensities for Stratified Interfaces. Fluorescence intensity $I^{ill}(z,\alpha)$ from an element i at a distance z from the air/water interface at an incidence angle α can be written as

$$I_i^f(\alpha) = S\int_0^\infty I^{ill}(z,\alpha)c_i(z)\exp\left(\frac{-z}{L_i}\right)dz \quad (3)$$

S is a proportional constant that is scaled out in our experimental system by the normalization to the fluorescence signal from the corresponding blank buffer and $c_i(z)$ is the concentration of element i at a depth z. The exponential term represents the attenuation of the fluorescence emission between the position z and the detector, where L_i is the attenuation length of water at the characteristic fluorescence line ($L_{Ni\ K\alpha}$ = 802.8 μm, $L_{S\ K\alpha}$ = 24.04 μm). The illumination profile $I^{ill}(z,\alpha)$ can be determined by the matrix propagation technique[19] using slab model.[20] Here, the determination of the electron density and the thickness of each slab from the XRR analysis are essential, since the illumination profile in a thin, stratified system is significantly influenced by the electronic structures. The concentration profile of the ion species was parametrized as

$$c_i(z) = c_0 + c_{max}\frac{\sqrt{e}(z - z_{HC})}{z_{max}}\exp\left(-\frac{(z - z_{HC})^2}{2z_{max}^2}\right) \quad (4)$$

where c_0 is the bulk concentration and z_{HC} is the chain/headgroup interface or the total thickness of the monolayer. This enabled us to model ion distributions that possess a concentration maximum with a smooth decay to the bulk concentration with only two free parameters: (i) the concentration maximum c_{max} and (ii) the z-position z_{max} of this maximum.[21] To refine the experimental results, we used the Levenberg–Marquardt nonlinear least-squares optimization in this study.[22]

RESULTS AND DISCUSSION

A. Phospholipid Monolayers Incorporating NTA Lipids. Figure 3A represents the XRR curves of SOPC monolayers incorporating 5 mol % (open circles), 25 mol % (open squares), and 50 mol % (open triangles) DOGS-NTA on Ni^{2+}-loaded buffer. For the fitting of the measured XRR curves, the SOPC/DOGS-NTA monolayer is modeled with a two-slab model: the first slab represents alkyl chains, and the second represents head groups. The best fit results and the reconstructed electron density (ρ) profiles in the direction perpendicular to the membrane plane are presented in Figures 3A (solid lines) and B, respectively. The thickness d, electron density ρ, and root-mean-square (rms) roughness σ of each interface are summarized in Table 1.

The thickness ($d \sim 12.8$ Å), electron density ($\rho \sim 0.2$ e × Å^{-3}), and roughness ($\sigma \sim 4$ Å) of alkyl chains of mixed monolayers exhibit no major dependence on the molar fractions of DOGS-NTA. On the other hand, the layer parameters of the headgroup region showed a small increase in the thickness and electron density of the headgroup/buffer interface along with the increase in the molar fractions of DOGS-NTA, which seems reasonable from increase in the lateral density of chelator (nitrilotriacetic acid) head groups with a higher electron density. The ideal mixing of two lipid components were further confirmed by the pressure–area

dx.doi.org/10.1021/jp401869t | J. Phys. Chem. B 2013, 117, 5002–5008

Table 1. Parameter of SOPC/DOGS-NTA Monolayers on Ni^{2+}-Loaded Buffer Corresponding to the Best Fits in Figure 3

5 mol % DOGS-NTA	d [Å]	ρ [e × Å^{-3}]	σ [Å]
alkyl chain	12.8	0.222	4.0
headgroup	8.6	0.435	4.1
buffer		0.336	2.9
25 mol % DOGS-NTA	d [Å]	ρ [e × Å^{-3}]	σ [Å]
alkyl chain	12.8	0.206	4.1
headgroup	8.7	0.451	3.8
buffer		0.336	5.8
50 mol % DOGS-NTA	d [Å]	ρ [e × Å^{-3}]	σ [Å]
alkyl chain	13.1	0.213	4.2
headgroup	9.7	0.451	3.9
buffer		0.336	5.0

isotherms, indicating that the excess Gibbs free energy of the lipid mixtures is almost zero (see Supporting Information).

Figure 4A shows the Ni^{2+}-Kα fluorescence intensities from SOPC monolayers incorporating 5 mol % (open circles), 25 mol % (open squares), and 50 mol % (open triangles) DOGS-NTA as a function of α_i, on Ni^{2+}-loaded buffer. It should be noted that the fluorescence signals from monolayers were always normalized to the corresponding signals from the blank buffer to exclude the influence of physical properties of fluorescence lines and other geometrical effects.

The penetration depth below the critical angle is a few nanometers and above it is in the micrometer range (see Supporting Information). This implies that fluorescence intensity below the critical angle is surface dominant while above it is dominated by the bulk. The fluorescence signal of Ni^{2+}-Kα collected at $\alpha_i < \alpha_c$ is stronger than that measured at $\alpha_i > \alpha_c$ for all the molar fractions, indicating the enrichment of Ni^{2+} ions near the air/water interface. Moreover, higher fluorescence intensity was detected by increasing the molar fraction of DOGS-NTA. In addition, the illumination profile spreads out as the incident angle increases and becomes closer to the critical angle (see Supporting Information). This makes the contribution of the fluorescence signal from the surface becoming less and gradually decays to the bulk level.

To analyze the experimental results with eq 3, the illumination intensity was calculated using the electronic structures of each slab obtained from XRR (Table 1). An asymmetric Gaussian function (eq 4) is used to model the concentration profiles of the Ni^{2+} ions. Figure 4B represents the concentration profiles corresponding to the best fit results presented as solid lines in Figure 4A by taking the bulk Ni^{2+} ion concentration of c_0 = 5 mM. As indicated by an arrow in Figure 4B, the onset of ion concentration profile (z_{HC} in eq 4) coincides with the thickness of alkyl chains, since z = 0 is defined as the chain/air interface in the XRR analysis. In the case of blank buffer, the fluorescence signal from ion depletion near the interface[23] is negligibly small and thus the experimental results can be well fitted with a constant concentration profile.

By integrating the excess concentration along the z-axis, one can estimate the lateral density (c_L) of Ni^{2+} ions. For example, in the case of SOPC monolayer doped with 5 mol % DOGS-NTA a lateral density of Ni^{2+} of $c_L = 7.9 \times 10^4$ ions/ μm^2 can be calculated. If one takes the average area per molecule of A = 58 Å^2 determined by pressure−area isotherms (See Supporting Information), the average area occupied by one NTA group would be 58/0.05 = 1160 Å^2. This yields the number of Ni^{2+} ions associated with one DOGS-NTA molecule N_{Ni} = 0.91 ± 0.25, implying that almost every NTA group forms a chelator complex. The maximum concentration of Ni^{2+}-ions (c_{max}), the stoichiometry of Ni^{2+}-NTA complex (N_{Ni}), and the peak position (z_{max}) are summarized in Table 2. A much lower

Table 2. The Lateral Density (c_L) of Ni^{2+} Ions, the Peak Position (z_{max}), the Maximum Concentration of Ni^{2+} Ions (c_{max}) and the Stoichiometry of Ni^{2+}-NTA Complex (N_{Ni})

	c_L [× 10^{12} ions/cm^2]	z_{max} [Å]	c_{max} [mM]	N_{Ni}
5 mol % DOGS-NTA	7.9	29	36.7 ± 3.7	0.91 ± 0.25
25 mol % DOGS-NTA	38.8	32	192.6 ± 26.2	0.94 ± 0.17
50 mol % DOGS-NTA	47.9	32	240.3 ± 11.0	0.63 ± 0.05

binding stoichiometry found for the monolayer with 50 mol % DOGS-NTA (N_{Ni} = 0.63 ± 0.05) suggests that some fraction of DOGS-NTA could make a complex consisting of one Ni^{2+} ion and two neighboring DOGS-NTA lipids. The 1:1 stoichiometry found at the molar fractions of 5 and 25 mol % seems to agree well with previous studies using atomic absorption spectroscopy[11] and isothermal titration calorimetry.[24] It should be noted

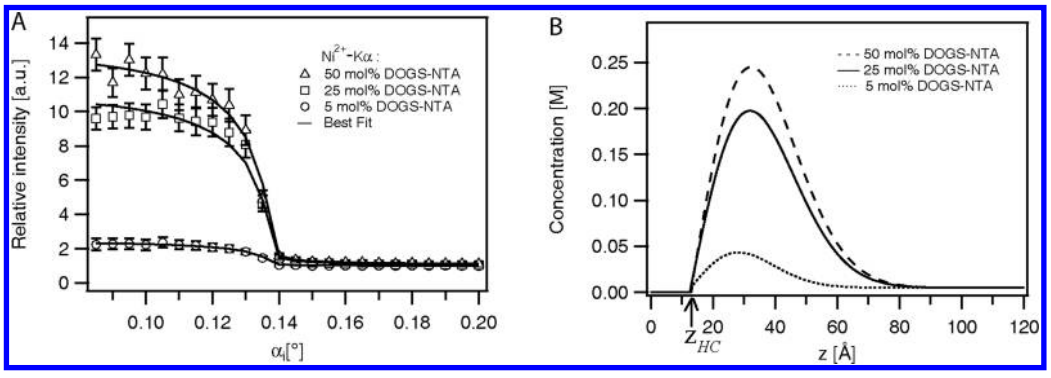

Figure 4. (A) Relative Ni^{2+}-Kα intensities from SOPC monolayers incorporating 5 mol % (open circles), 25 mol % (open squares), and 50 mol % (open triangles) DOGS-NTA on Ni^{2+}-loaded buffer, measured at α_i below and beyond the critical angle of total reflection. Error bars coincide with standard deviations from the Gaussian error propagation during the fitting. The solid lines indicate the best fit results to the experimental data. (B) The ion concentration profiles normal to the air/water interface, reconstructed from the best fit results.

dx.doi.org/10.1021/jp401869t | J. Phys. Chem. B 2013, 117, 5002−5008

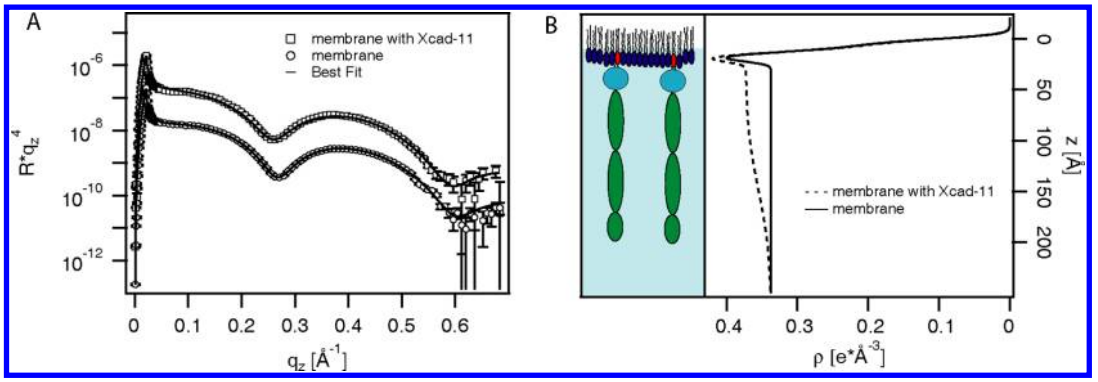

Figure 5. (A) Specular X-ray reflectivity curves of a monolayer doped with 5 mol % DOGS-NTA before (open circles) and after (open squares) the binding of Xcad-11, measured on Ni^{2+}-free buffer. The solid lines represent the best fit models matching the experimental results. (B) The reconstructed electron density profiles in the direction perpendicular to the air/water interface.

that the former study deals with NTA groups covalently coupled to glass surface and the latter with NTA groups in bulk solution. In contrast, the combination of XRR and GIXF at the air/water interface enables us to precisely control the lateral density of NTA groups and quantitatively determine the binding stoichiometry. Moreover, the combination of XRR and GIXF allows for the localization of the target element within Å accuracy. In fact, the peak position of Ni^{2+} concentration profile was found at Z_{max} = 29 ± 5 Å for the monolayer with 5 mol % DOGS-NTA. A slight shift to a higher distance at higher molar fractions Z_{max} = 32 ± 5 Å agrees well with XRR results.

B. Coupling of Histidine-Tagged X-cad 11 to Lipid Monolayers. Figure 5A,B represents the XRR curves and the reconstructed electron density profiles of the lipid monolayer incorporating 5 mol % DOGS-NTA before (open circles) and after (open squares) the binding of Xcad-11, measured on Ni^{2+}-free buffer. As presented in Table 3, the layer parameters of a monolayer (open circles) on Ni^{2+}-free buffer obtained from the best fit model (solid line) are almost identical to the corresponding values collected on Ni^{2+}-loaded buffer (Table 1), verifying that the stoichiometry of chelator complexes is identical to that on Ni^{2+}-loaded buffer.

Table 3. Parameter of SOPC/DOGS-NTA Monolayer with and without Xcad-11 EC1-3 from the Best Fits in Figure 5

5 mol % DOGS-NTA (membrane)	d [Å]	ρ [e × Å^{-3}]	σ [Å]
alkylchain	13.0	0.206	3.8
headgroup (SOPC,DOGS-NTA-Ni)	8.3	0.444	4.4
water		0.336	3.2
membrane + Xcad-11 EC 1-3	d [Å]	ρ [e × Å^{-3}]	σ [Å]
alkylchain	13.1	0.201	3.9
headgroup (SOPC,DOGS-NTA-Ni)	8.8	0.454	4.3
X-Cad11 (EC 1-3)	126.5	0.373	3
water		0.336	50.0

Prior to the XRR measurement in the presence of Xcad-11 (open circles), the monolayer was incubated with Xcad-11 in Ni^{2+}-free buffer (final concentration: 10 μg/mL) for 6 h to ensure that the system reached to thermodynamic equilibrium. The surface pressure of the monolayer remained constant after the injection and incubation of Xcad-11 solutions, which confirms that the change in fine structures was not caused by the physisorption of surface active proteins. As presented in Figure 5B and Table 3, the binding of Xcad-11 results in a major change in the monolayer structures, which can be modeled by inserting an additional slab. It should be noted that the binding of Xcad-11 to the membrane did not cause any remarkable change in the thickness, electron density, and interface roughness for both alkyl chains and head groups. This suggests that Xcad-11 molecules are bound to the membrane surface but are not integrated into the membrane core. The calculated thickness of recombinant Xcad-11 layer at the air/water interface, 127 ± 3 Å, is in good agreement with what we recently measured at the solid/liquid interface by the use of high energy X-ray, 126 Å.[25] This value actually seems plausible, since our recombinant contains only two adhesion domains (EC 1-3) of the whole cadherin (EC 1-5) molecule that has a full length of ~220 Å.[26] The electron density (ρ) of the protein layer, 0.373 e × Å^{-3}, agrees well with the previously reported one for different cadherins.[25,27] The apparently larger roughness of Xcad-11/water interface (50 ± 1 Å) than the other interfaces can be attributed to the fact that the Xcad-11 "layer" is composed of a lateral assembly of rodlike cadherin.

Figure 6A shows the relative S Kα fluorescence intensities from a SOPC monolayer doped with 5 mol % DOGS-NTA 6 h after the injection of Xcad-11 (open circles). To obtain the concentration profile of S atoms, the illumination profile through a lipid monolayer functionalized with proteins was calculated using the electronic structures obtained from XRR (Table 3). Like the case of a monolayer in the absence of proteins, the z_{HC} value in eq 4 is the total thickness of alkyl chain and the headgroup obtained by XRR (d = 13.1 + 8.8 Å = 21.9 Å, Table 3). The ion concentration profile reconstructed from the best fit result (Figure 6A) is presented in Figure 6B in which the maximum concentration of S atoms can be found at Z_{max} = 68 ± 16 Å. The estimated peak position seems reasonable from the structure of recombinant Xcad-11,[27] since the part adjacent to the histidine-tag (hAGT)[28] contains more S atoms (9) than the following EC 1-3 Domain (6).

Despite the high accuracy in the spatial localization of the peak position achieved here, it should be noted that the intensity below the critical angle of incidence was only by a factor of 2 stronger than the bulk level. This is in contrast to our previous study on neutravidin, where the intensity at $\alpha_i < \alpha_c$ was about 4 − 6 times stronger than that from bulk.[20] This makes it very challenging to precisely determine the c_{max} value, since it strongly depends on the intensity level at $\alpha_i < \alpha_c$. The integration of the area below the curve in Figure 6B yields a lateral concentration of S atoms of (2.7 ± 0.3) × 10^{-11} mol/cm^2. With the total number of S atoms in recombinant Xcad-11 (15), the area occupied by one recombinant His12 molecule

dx.doi.org/10.1021/jp401869t | J. Phys. Chem. B 2013, 117, 5002−5008

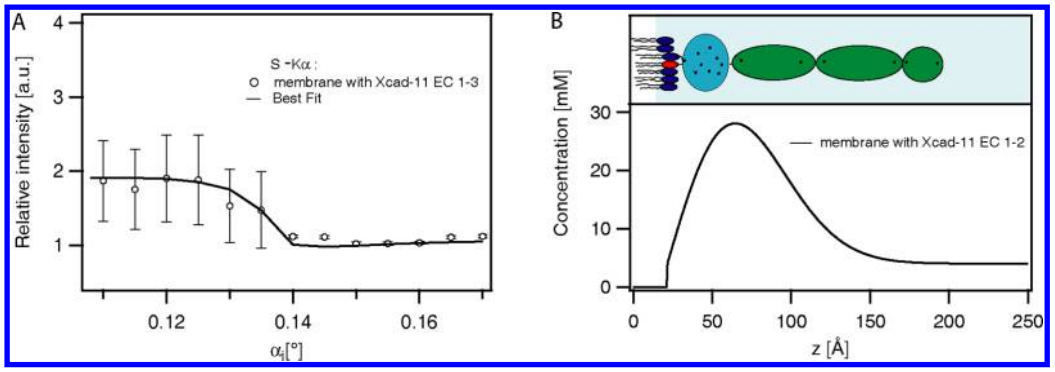

Figure 6. (A) Relative S Kα intensities from SOPC monolayers incorporating 5 mol % DOGS-NTA after the binding of Xcad-11 (open circles) as a function of α_i on Ni^{2+}-free buffer. Vertical bars are ± standard deviations obtained from Gaussian error propagation during the fit of the fluorescence spectra. The solid lines indicate the best fit to the experimental data. (B) The ion concentration profile normal to the interface reconstructed from the best fit results.

can be estimated to be ~90 nm^2, which is about 6 times smaller than the value expected from the lateral density of lipid anchors. Currently, a distinct difference in the sensitivity between Xcad-11 and neutravidin would be attributed to the fact that S atoms of Xcad-11 are much broadly distributed near the interface than those of neutravidin.

CONCLUSIONS

This account demonstrates that the combination of GIXF and XRR enables one to quantitatively determine the density profiles of metal ions as well as S atoms near the air/water interface. The quantitative analysis of GIXF from lipid monolayers incorporating lipids with NTA head groups sensitively detected a remarkable accumulation of Ni^{2+} ions near the air/water interface. Moreover, the integration of ion concentration profiles yields the surface concentration of Ni^{2+} ions. From the linear relationship between the molar fractions of NTA lipids and the surface concentration of Ni^{2+} ions, we demonstrated that >0.9 Ni^{2+} forms a chelator complex with one NTA lipid at the molar fraction of 5 and 25 mol %. As a biologically recombinant protein, we selected histidine-tagged XCad-11 (Xcad-11) that plays key roles in cell adhesion and migration of neural crest cells. The coupling of histidine-tagged *Xenopus* cadherin 11 (Xcad-11) can also be identified by changes in the fines-structures using XRR. As fluorescence intensities from S Kα level at $\alpha < \alpha_c$ were much weaker than Ni Kα signals, we could not precisely determine the lateral concentration of S atoms and thus the lateral density of proteins at the interface. On the other hand, we could sensitively detect the location of S atoms in proteins, which cannot be assessed only by XRR. The obtained results demonstrated that the unique combination of XRR and GIXF enables one to quantify not only the electron density profiles but also density profiles and lateral density of target elements in biologically functionalized lipid membranes.

ASSOCIATED CONTENT

Supporting Information

Background subtraction, pressure−area isotherms of SOPC/DOGS-NTA monolayers, the cancellation of Ni^{2+}-NTA chelator complexes, and quantitative determination of the Ni^{2+}-NTA complex binding stoichiometry. This material is available free of charge via the Internet at http://pubs.acs.org.

AUTHOR INFORMATION

Corresponding Author

*Tel: +49-(0)-6221-544916. Fax: +49-(0)-6221-544918. E-mail: tanaka@uni-heidelberg.de.

Notes

The authors declare no competing financial interest.

ACKNOWLEDGMENTS

A.K., F.F.R., O.V.K, and M.T. thank ESRF for synchrotron beam time. D.W. and M.T. are the members of the Helmholtz program "BioInterfaces". M.T. is a member of German Cluster of Excellence "Cell Network". F.F.R. is thankful to the DFG for the research fellowship (RO 3643/1-1). We thank S. Afonin from the Biochemistry at the Karlsruhe Institute of Technology (KIT) for kind help with MALDI analysis and Jubin Kashef and Dagmar Fichtner for construction of Xcad-11-SNAP-His construct. W.A. is thankful to the graduate college program GRK1114 supported by the German Science Foundation. This work was supported by the Heidelberger Academy of Science (WINKolleg BioForm) and the Helmholtz Society (Bio-Interfaces programm).

ABBREVIATIONS

GIXF, grazing incidence X-ray fluorescence; XRR, specular X-ray reflectivity; Xcad-11, *Xenopus* cadherin 11 EC 1−3 Snap His12; NTA, nitrilotriacetic acid; SOPC, stearoyl-oleoyl-phosphatidylcholine

REFERENCES

(1) Kjaer, K.; Alsnielsen, J.; Helm, C. A.; Laxhuber, L. A.; Mohwald, H. Ordering in Lipid Monolayers Studied by Synchrotron X-Ray-Diffraction and Fluorescence Microscopy. *Phys. Rev. Lett.* **1987**, *58*, 2224−2227.

(2) McConnell, H. M.; Tamm, L. K.; Weis, R. M. Periodic Structures in Lipid Monolayer Phase Transitions. *Proc. Natl. Acad. Sci. U.S.A.* **1984**, *81*, 3249−3253.

(3) Albrecht, O.; Gruler, H.; Sackmann, E. Pressure Composition Phase Diagrams of Cholesterol Lecithin Cholesterol Phosphatidic-Acid and Lecithin Phosphatidic-Acid Mixed Mono Layers a Langmuir Film Balance Study. *J. Colloid Interface Sci.* **1981**, *79*, 319−338.

(4) Henon, S.; Meunier, J. Microscope at the Brewster Angle: Direct Observation of First-Order Phase Transitions in Monolayers. *Rev. Sci. Instrum.* **1991**, *62*, 936−939.

(5) Hoenig, D.; Moebius, D. Direct Visualization of Monolayers at the Air-Water Interface by Brewster Angle Microscopy. *J. Phys. Chem.* **1991**, *95*, 4590−4592.

(6) Maggio, B. The Surface Behavior of Glycosphingolipids in Biomembranes - a New Frontier of Molecular Ecology. *Prog. Biophys. Mol. Biol.* **1994**, *62*, 55−117.
(7) McCormick, D. B. Specific Purification of Avidin by Column Chromatography on Biotin-Cellulose. *Anal. Biochem.* **1965**, *13*, 194−198.
(8) Porath, J.; Carlsson, J. A. N.; Olsson, I.; Belfrage, G. Metal Chelate Affinity Chromatography, a New Approach to Protein Fractionation. *Nature* **1975**, *258*, 598−599.
(9) Finn, F. M.; Titus, G.; Horstman, D.; Hofmann, K. Avidin-Biotin Affinity Chromatography Application to the Isolation of Human Placental Insulin Receptor. *Proc. Natl. Acad. Sci. U.S.A.* **1984**, *81*, 7328−7332.
(10) Grabowski, P. J.; Sharp, P. A. Affinity Chromatography of Splicing Complexes U-2 U-5 and U-4 Plus U-6 Small Nuclear Ribonucleoprotein Particles in the Spliceosome. *Science* **1986**, *233*, 1294−1299.
(11) Hochuli, E.; DÃ¶beli, H.; Schacher, A. New Metal Chelate Adsorbent Selective for Proteins and Peptides Containing Neighbouring Histidine Residues. *J. Chromatogr., A* **1987**, *411*, 177−184.
(12) Schmitt, L.; Dietrich, C.; Tampe, R. Synthesis and Characterization of Chelator-Lipids for Reversible Immobilization of Engineered Proteins at Self-Assembled Lipid Interfaces. *J. Am. Chem. Soc.* **1994**, *116*, 8485−8491.
(13) Kashef, J.; Koehler, A.; Kuriyama, S.; Alfandari, D.; Mayor, R.; Wedlich, D. Cadherin-11 Regulates Protrusive Activity in Xenopus Cranial Neural Crest Cells Upstream of Trio and the Small Gtpases. *Genes Dev.* **2009**, *23*, 1393−1398.
(14) Borchers, A.; David, R.; Wedlich, D. Xenopus Cadherin-11 Restrains Cranial Neural Crest Migration and Influences Neural Crest Specification. *Development* **2001**, *128*, 3049−3060.
(15) Juillerat, A.; Gronemeyer, T.; Keppler, A.; Gendreizig, S.; Pick, H.; Vogel, H.; Johnsson, K. Directed Evolution of O6-Alkylguanine-DNA Alkyltransferase for Efficient Labeling of Fusion Proteins with Small Molecules in Vivo. *Chem. Biol.* **2003**, *10*, 313−317.
(16) Parratt, L. G. Surface Studies of Solids by Total Reflection of X-Rays. *Phys. Rev.* **1954**, *95*, 359−369.
(17) Nelson, A. Co-Refinement of Multiple-Contrast Neutron/X-Ray Reflectivity Data Using Motofit. *J. Appl. Crystallogr.* **2006**, *39*, 273−276.
(18) Yun, W. B.; Bloch, J. M. X-Ray near Total External Fluorescence Method - Experiment and Analysis. *J. Appl. Phys.* **1990**, *68*, 1421−1428.
(19) Ohta, K.; Ishida, H. Matrix Formalism for Calculation of Electric-Field Intensity of Light in Stratified Multilayered Films. *Appl. Opt.* **1990**, *29*, 1952−1959.
(20) Abuillan, W.; Vorobiev, A.; Hartel, A.; Jones, N. G.; Engstler, M.; Tanaka, M. Quantitative Determination of the Lateral Density and Intermolecular Correlation between Proteins Anchored on the Membrane Surfaces Using Grazing Incidence Small-Angle X-Ray Scattering and Grazing Incidence X-Ray Fluorescence. *J. Chem. Phys.* **2012**, 137.
(21) Schneck, E.; Schubert, T.; Konovalov, O. V.; Quinn, B. E.; Gutsmann, T.; Brandenburg, K.; Oliveira, R. G.; Pink, D. A.; Tanaka, M. Quantitative Determination of Ion Distributions in Bacterial Lipopolysaccharide Membranes by Grazing-Incidence X-Ray Fluorescence. *Proc. Natl. Acad. Sci. U.S.A.* **2010**, *107*, 9147−9151.
(22) Boggs, P. T.; Donaldson, J. R.; Byrd, R. H.; Schnabel, R. B. Odrpack - Software for Weighted Orthogonal Distance Regression. *Assoc. Comput. Machin. Trans. Math. Software* **1989**, *15*, 348−364.
(23) Padmanabhan, V.; Daillant, J.; Belloni, L.; Mora, S.; Alba, M.; Konovalov, O. Specific Ion Adsorption and Short-Range Interactions at the Air Aqueous Solution Interface. *Phys. Rev. Lett.* **2007**, *99*, 086105.
(24) Stora, T.; Hovius, R.; Dienes, Z.; Pachoud, M.; Vogel, H. Metal Ion Trace Detection by a Chelator-Modified Gold Electrode: A Comparison of Surface to Bulk Affinity. *Langmuir* **1997**, *13*, 5211−5214.
(25) Körner, A.; Deichmann, C.; Rossetti, F. F.; Köhler, A.; Konovalov, O. V.; Wedlich, D.; Tanaka, M. Cell Differentiation of Pluripotent Tissue Sheets Immobilized on Supported Membranes Displaying Cadherin-11. *PLoS One* **2013**, *8*, e54749.
(26) Pokutta, S.; Herrenknecht, K.; Kemler, R.; Engel, J. Conformational Changes of the Recombinant Extracellular Domain of E-Cadherin Upon Calcium Binding. *Eur. J. Biochem.* **1994**, *223*, 1019−26.
(27) Patel, S. D.; Ciatto, C.; Chen, C. P.; Bahna, F.; Rajebhosale, M.; Arkus, N.; Schieren, I.; Jessell, T. M.; Honig, B.; Price, S. R.; et al. Type Ii Cadherin Ectodomain Structures: Implications for Classical Cadherin Specificity. *Cell* **2006**, *124*, 1255−1268.
(28) Daniels, D. S.; Mol, C. D.; Arvai, A. S.; Kanugula, S.; Pegg, A. E.; Tainer, J. A. Active and Alkylated Human Agt Structures: A Novel Zinc Site, Inhibitor and Extrahelical Base Binding. *EMBO J.* **2000**, *19*, 1719−1730.